Control of H-related defects in γ-MnO_2 in a hydrothermal synthesis

Nicolas P. L. Magnard[1], Andrea Kirsch[1], Mads R. V. Jørgensen[2,3], Innokenty Kantor[2,4], Daniel R. Sørensen[2,3], Simo Huotari[5], Svemir Rudić[6], Heloisa N. Bordallo[7] and Kirsten M. Ø. Jensen[1]*

1: Department of Chemistry, University of Copenhagen, Denmark

2: MAX IV Laboratory, Lund, Sweden

3: Department of Chemistry & iNANO, Aarhus University, Denmark

4: Department of Physics, Technical University of Denmark, Denmark

5: Department of Physics, University of Helsinki, Finland

6: ISIS Neutron and Muon Source, STFC, Rutherford Appleton Laboratory, Didcot, United Kingdom

7: Niels Bohr Institute, University of Copenhagen, Denmark

*Correspondence to: kirsten@chem.ku.dk

Abstract

Manganese dioxide is a good candidate for effective energy storage and conversion as it possesses a rich electrochemistry. The compound also shows a wide polymorphism. The γ-variety, an intergrowth of β- and R-MnO_2, has been extensively studied in several types of batteries (e.g. Zn/MnO_2, Li-ion) and is a common electrode material for commercial batteries. It is well known that the insertion of protons thermodynamically stabilises γ-MnO_2 with respect to β-MnO_2. Protons can enter the structure either by forming groups of 4 hydroxyls around a Mn^{4+} vacancy, called a Ruetschi defect, or by forming a hydroxyl group near a Mn^{3+} ion, called a Coleman defect. These defects differently affect the electrochemistry of manganese oxide, and tailoring their amount in the structure can be used to tune the material properties. Previous studies have addressed the proton insertion process, but the role of the synthesis pathway on the amount of defects created is not well understood. We here investigate how the parameters in a hydrothermal synthesis of γ-MnO_2 nanoparticles influence the amount and type of H-related defects. Structural investigations are carried out using Pair Distribution Function analysis, X-ray absorption spectroscopy, thermogravimetric analysis, and inelastic neutron scattering. We demonstrate the possibility to control the amount and type of defects introduced during the synthesis. While the amount of Ruetschi defects increases with synthesis temperature, it decreases with extended synthesis time, along with the amount of Coleman defects. Moreover, we discuss the arrangement of the defects in the γ-MnO_2 nanoparticles.

Introduction

Manganese oxides have been widely studied for their electrochemical properties. They are used as electrode materials for e.g. Zn/MnO_2,[1,2] Li-, and Na-ion batteries,[3,4] but also as catalysts for the removal of volatile organic compounds[5-8] and the oxygen evolution reaction.[9,10] The superior electrochemical performance arises due to the stability of the manganese ion in several oxidation states. Manganese ions can be commonly found in oxidation states +II, +III and +IV, giving rise to diverse oxides of compositions ranging from MnO to MnO_2. Furthermore, manganese dioxide MnO_2 shows a rich polymorphism with structures based on a versatile assembly of [MnO_6] octahedra forming layered or tunnel structures.[11] The most thermodynamically stable variety is β-MnO_2. It crystallises in a rutile structure (Figure 1c), where the octahedra form edge-sharing chains along the c-axis, which connect via corner-sharing to form a tunnel structure with dimensions of (1X1) along the a- and b-axis. Larger tunnel structures can be stabilised by insertion of alkali or alkali-earth ions,[12] but also by protons H^+. For example, proton insertion leads to a lowering of the Gibbs free-energy of the R- and γ-MnO_2 varieties.[12,13] R-MnO_2 shows a (2x1) tunnel structure (Figure 1b) and γ-MnO_2 is an intergrowth between β- and R-MnO_2[12] (Figure 1a). The stabilisation

of these phases occurs in two distinct ways, either through the substitution of Mn^{4+} and O^{2-} by Mn^{3+} and $(OH)^-$, called Coleman defects,[14] or by the substitution of a Mn^{4+} ion by four protons, called Ruetschi defects.[14] The different types of defects in γ-MnO_2 are illustrated in Figure 1, where the Coleman defects can be interpreted as local γ-MnOOH (Figure 1d) or α-MnOOH (Figure 1e) domains within the γ-MnO_2 structure. Ruetschi defects can be represented by four $(OH)^-$ groups clustered around a Mn^{4+} vacancy (Figure 1f). Coleman and Ruetschi defects have been extensively studied[13-17] for the role they play in the electrochemical properties of γ-MnO_2.[4] It has been shown that Ruetschi defects are beneficial for the cycling stability in γ-MnO_2 batteries due to a lowering of its overpotential.[13,18] In turn, Coleman defects are detrimental to the electrode life-time as they irreversibly lead to the formation of Mn_3O_4, which hampers the cyclability of the material.[1,2,15,18] Nevertheless, Coleman defects may be interesting for electrocatalysis as several studies have shown a significant role of Mn^{3+} in catalytic processes, e.g. in the oxygen evolution reaction (OER).[19-21] Thus, controlling the amount and type of these defects in γ-MnO_2 would allow to develop materials for targeted applications.

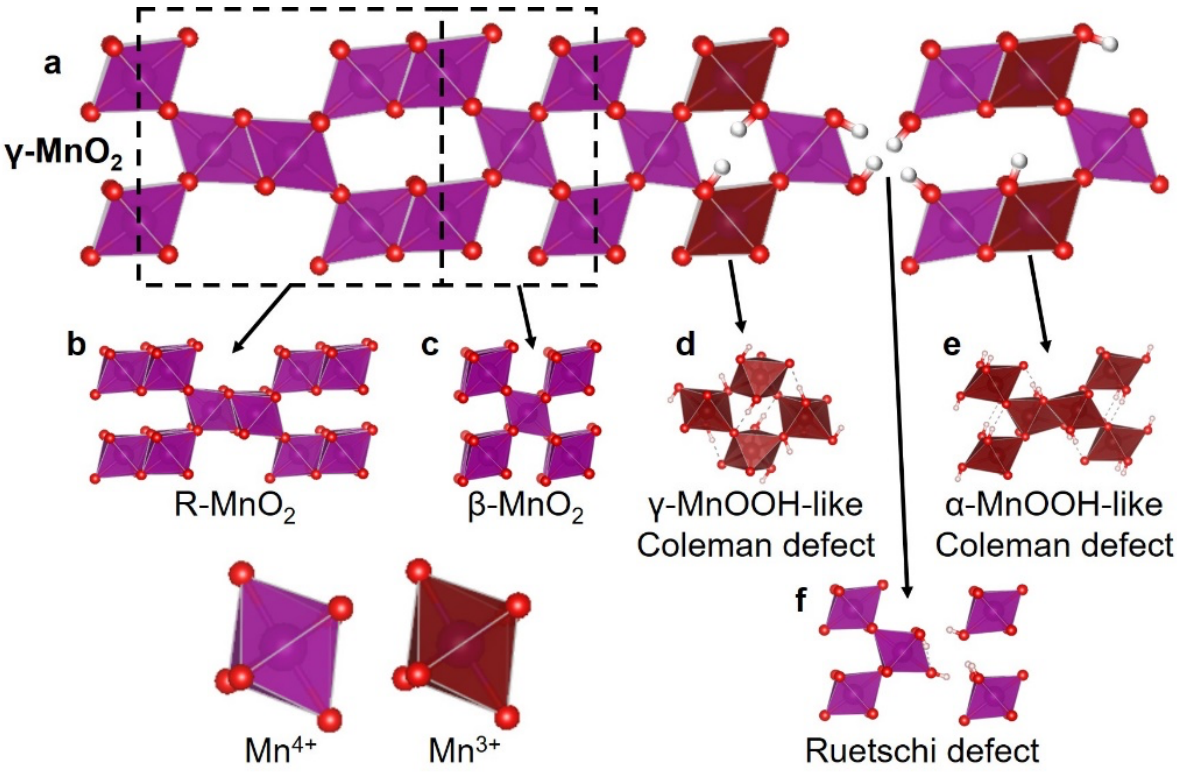

Figure 1: Description of the different types of defects in γ-MnO_2. a) γ-MnO_2 representing an intergrowth of the parent structures b) R-MnO_2 and c) β-MnO_2. Defects involving protons can form in both parent structures by forming Coleman defects, i.e. local MnOOH domains structurally similar to d) γ-MnOOH and e) α-MnOOH, isostructural to β- MnO_2 and R-MnO_2. f) Ruetschi defects in R-MnO_2, i.e. 4 $(OH)^-$ groups clustered around a manganese vacancy. Mn^{4+} atoms are shown in purple, Mn^{3+} in brown, O atoms in red and H atoms in white.

Several characterisation methods can be used to study the presence and nature of defects in MnO_2. Hydrogen-related defects in γ-MnO_2 are related to the presence of hydroxyl groups $(OH)^-$ in the structure. They can be minimised by thermal treatment of the sample,[22] as water molecules are released from the structure. Tracking mass loss during a thermal treatment by thermogravimetric analysis (TGA) can therefore provide information on the presence of these defects. The technique has previously been used to study structural water and hydroxyls in oxide compounds,[23,24] including γ-MnO_2[22] and γ-MnOOH.[25] Neutrons are

also an excellent probe for the investigation of hydrogen-related defects in these materials. H^1 atoms have a neutron incoherent cross-section several orders of magnitude higher than manganese and oxygen, i.e. 80.26 (H^1), 0.4 (Mn) and 0.0008 (O) barn. Similar to Raman and infrared spectroscopy, inelastic neutron scattering (INS) probes vibrational modes in a system by energy transfer between the atoms in a system and the neutron beam, however without selection rules.[26,27] INS can therefore provide great insight into the different hydrogen environments in γ-MnO_2 and allows investigating Coleman and Ruetschi defects.[16]

Beside the insertion of hydrogen atoms into the structure, Coleman defects involve the substitution of a Mn^{4+} ion by Mn^{3+}. The change in oxidation state of Mn can be probed by X-ray Absorption Near-Edge Spectroscopy (XANES). XANES provides element specific information about the local environment of a given atom and is sensitive to oxidation states making it excellently suited to study systems containing transition metal oxides, which can have several oxidation states within a single material. The structure of nanomaterials can be investigated using X-ray total scattering and Pair Distribution Function (PDF) analysis as both the Bragg and diffuse scattering are analysed.[28] PDF is ideal for studying local structures in disordered materials and nanoparticles since it provides structural information at the long range, but also in the range of the first atomic pairs. PDF analysis has previously been used to characterise γ-MnO_2.[29] For example, we used a combination of PDF and PXRD with structure mining to quantify the amount of intergrowth defects in γ-MnO_2.[30]

Powder samples of γ-MnO_2 are commonly synthesised using hydrothermal synthesis. This synthesis route is inexpensive and scalable, easy to implement, and allows to obtain various polymorphs of the same compound by tuning synthesis parameters. The defective structure of γ-MnO_2 of hydrothermally synthesised particles has previously been characterised by several techniques including neutron powder diffraction,[31] INS,[16,32] XANES,[33] and *ab initio* calculations.[13,15,18,34,35] However, how these defects form and how their presence is affected by the synthesis parameters is not yet well understood. Here, we study how the variation of parameters in a hydrothermal synthesis influences the proton insertion into the γ-MnO_2 structure by combining PDF analysis with TGA, XANES and INS. We find that increasing the temperature reduces the amount of Coleman defects and promotes the formation of Ruetschi defects, while increasing the synthesis time reduces the amount of both type of defects. Moreover, we show that both the synthesis temperature and time influence the way the defects arrange in the microstructure.

Methods

γ-MnO_2 samples were synthesised hydrothermally based on the protocol of Wang et al.[36] 3.5 mmol of $MnSO_4 \cdot H_2O$ (Sigma Aldrich, 99%) and 1.75 mmol of $(NH_4)_2S_2O_8$ (Sigma Aldrich, 99%) were dissolved in 5 mL of water in a 23 mL teflon-lined steel autoclave. Three samples were produced at 120 °C for 2 h (sample A), 80 °C for 3 h (sample B), and 80 °C for 6 h (sample C). After the heating process, the autoclave was taken out of the oven to cool down to room temperature. The formed black precipitate was filtered and washed three times with water and ethanol and left to dry at room temperature. The black powder was ground in an agate mortar before characterisation.

X-ray total scattering experiments were carried out at the DanMAX beamline, MAX IV Laboratory in Lund, Sweden on samples packed in 1 mm Kapton capillaries. The data were collected with an X-ray wavelength of 0.3542 Å and a DECTRIS PILATUS3 X CdTe 2M area detector with a sample detector distance of ca. 100 mm. The total scattering patterns were integrated using Dioptas[37] and the corresponding PDFs obtained using xPDFSuite.[38] The scattering pattern of an empty Kapton capillary was used for background subtraction. The PDF patterns were modelled and refined with Topas Academic.[39]

XANES spectra of the Mn K-edge were measured at the Center for Spectroscopy at the University of Helsinki on HelXAS.[40] The powder samples were diluted using cellulose and mixed in ethanol. The resulting slurry was pelletised and left to dry. The spectra were acquired at X-ray energies ranging from 6525 to 6625 eV. The XANES signal was normalised with respect to the incident beam intensity. First, spectra of

an elemental Mn foil and a powder of pure commercial β-MnO_2 were acquired and their corresponding edge position was extracted by analysis of the first derivative of the spectra.

Thermogravimetric analysis was carried out using a Neztsch TG 209 F1 Libra. About 20 mg of sample was placed in an alumina crucible and introduced into the furnace chamber in which a continuous N_2 flow of 20 ml/min was applied throughout the whole experiment. When the furnace chamber temperature was stabilised, the samples were heated up to 600 °C using a heating rate of 10 K/min.

INS spectra were collected at the TOSCA[41] neutron spectrometer at ISIS Neutron and Muon Source at Oxfordshire, United Kingdom. To avoid scattering signal from water, the samples were dried overnight at 80 °C before measurements. The samples were placed in an aluminum can and cooled down to 20 K. The INS spectra of each sample were collected for 12 hours. The background signal from the aluminum can was subtracted and the resulting spectra were normalised by the mass of each sample.

Results and discussion

Quantification of Coleman and Ruetschi defects in γ-MnO_2

We first use X-ray total scattering to confirm the structure of the three samples. As shown from diffraction patterns in Figure S1, all three γ-MnO_2 samples are close to the parent structure R-MnO_2. This implies that the samples mainly contain (2x1) tunnels (see Figure 1b). However, differences in relative intensities between experimental and theoretical data can be observed in the 110 and 221 reflections at 1.56 $Å^{-1}$ and 3.82 $Å^{-1}$. This observation indicates that our samples deviate from the ideal R-MnO_2 structure.

PDF analysis shows similarities between samples, as the three PDFs show peaks at the same position with intensities of similar magnitude as illustrated in Figure 2a. However, some subtle variations can be observed, e.g. the relative intensity and position of peaks in the low-r region as emphasised in Figure 2b. These peaks can be assigned to the Mn-O bond in [MnO_6] octahedra (1.9 Å), and Mn-Mn in edge-sharing (2.8 Å) and corner-sharing (3.4 Å) octahedra (Figure 2c).

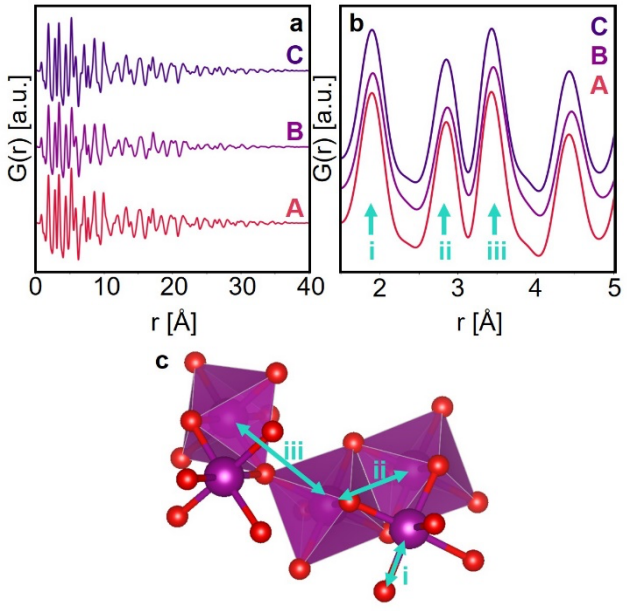

Figure 2: Local structure of the γ-MnO_2 samples. a) PDFs of samples A (red), B (purple) and C (blue). b) Magnification of the low-r region of the PDFs shown in a). c) Illustration of the three first pair distances observed in the PDF. These correspond to Mn-O (i), Mn-Mn between edge-sharing (ii) and corner-sharing (iii) [MnO_6] octahedra.

The PDFs can be further analysed through modelling. We first use the R-MnO_2 structure as model in a single-phase fit. However, this structure cannot fully describe the experimental PDFs, as shown in Figure S2a and Table S1. For instance, the intensity of the peak at 3.4 Å, corresponding to the Mn-Mn distance between two corner-sharing octahedra, is not fully accounted for by the R-MnO_2 model. A misfit is generally seen across the fitted range. Since γ-MnO_2 is an intergrowth of R- and β-MnO_2, we next tried a model comprising both phases, where parameters from both structures are refined simultaneously as done by Galliez et al.[29] The results from these refinements are shown in Figure S2b and Table S2. The refinements show that the addition of the β-MnO_2 phase did not improve the fits compared to those performed using only R-MnO_2. Again, the PDF peak intensities are not well described.

Manganese oxides, especially γ-MnO_2, are prone to form defects and thereby the misfit is likely associated to their presence in the structure. As described above, the presence of Coleman defects manifests in the local structure of the γ-MnO_2 phase as oxyhydroxide (α-MnOOH or γ-MnOOH) domains. By including such nanodomains in the refinements, it may thus be possible to quantify the amount of Coleman defects in the samples. Due to the close structural similarities between R-MnO_2 and α-MnOOH, i.e. same space group (*Pnam*) and atomic sites, α-MnOOH was not included in the refinements, and only γ-MnOOH was used to account for Coleman defects. The refined weight fractions of R-MnO_2 and γ-MnOOH are reported in Table S3 and the PDFs fits shown in Figure 3a-c. Generally, the addition of γ-MnOOH clearly improves the fit. Manganese ions in oxidation state +III undergo Jahn-Teller (JT) distortions[42] and the addition of a γ-MnOOH phase allows to account for the splitting of the first peak below 2.0 Å in the PDF, relating to Mn-O distances. The local range of the PDFs is now well described up to 20 Å, however peak positions begin to deviate in the middle and long range. The domain size (sp-diameter) for both the γ-MnOOH and R-MnO_2 structure refine to ca. 3-4 nm. γ-MnO_2 structures are known to display some microtwinning along the 102 and 106 planes.[43] These defects are not taken into account in the present modelling, but may affect the PDF fit. The nanostructure of the sample, i.e., the position and distribution of defects are also likely to affect the fit.

Since we account for Coleman defects using the γ-MnOOH structure, we assume that its weight fraction directly relates to the defect concentration in the sample. The refined phase fraction of oxyhydroxide γ-MnOOH decreases from sample B to C (26.3 and 21.3 %, Table S3), i.e. when the reaction time is increased from 3 h (sample B) to 6 h (sample C). However, it is lowest in sample A (19.2 %, Table S3), suggesting a further decrease of the amount of Coleman defects when the reaction is carried out at a higher temperature (120 °C, sample A vs 80 °C, sample B and C). While the refined cell parameters of R-MnO_2 are close to the ones of the bulk phase, the ones of γ-MnOOH deviate significantly from the bulk phase, e.g. b = 4.79 Å (A) vs. b = 5.27 Å (bulk γ-MnOOH) (Table S3). We relate these effects to the nanostructure of the samples, as will be discussed further below.

Previous studies have shown that Ruetschi defects, i.e. manganese vacancies in the structure, occur in the range of 1-4 atomic percent.[12,14] Such a low amount of defects in this complex system makes their quantification difficult by PDF analysis. Thus, Ruetschi defects were not considered further in the PDF analysis.

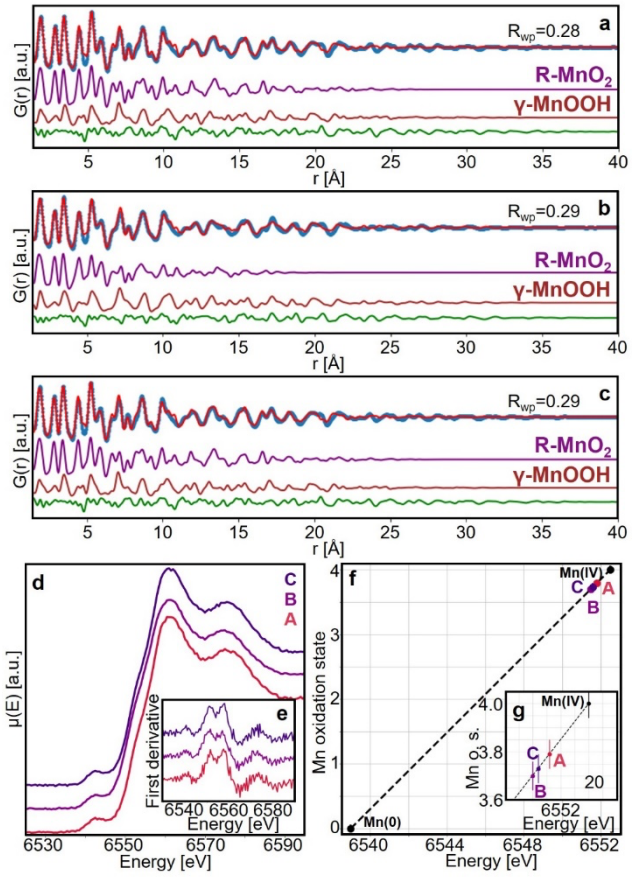

Figure 3: PDF refinements of samples a) A, b) B, and c) C using the R-MnO_2 (*Pnam*) and γ-MnOOH ($P2_1/c$) structures. The experimental PDF is shown in blue dots, the refined model in red solid line and difference curve in green solid line. The contribution of the R-MnO_2 and γ-MnOOH phase is shown in purple and brown, respectively. d) XANES spectra at the Mn K-edge of samples A, B and C. e) First derivative of the XANES spectra. f) The edge position of each spectrum is extracted and plotted against the average oxidation state of manganese in each sample. g) Magnification of the high oxidation region of f).

We further investigated the Coleman defects by performing XANES at the Mn K-edge. The resulting spectra are shown in Figure 3d. This technique is sensitive to the oxidation state of the probed element and allows extracting the average oxidation state of manganese in the samples. As for other transition metal oxides,[44-46] the manganese oxidation state is linearly correlated with the energy shift of some of the XANES features and the edge position can be directly related to the manganese valence. By measuring XANES spectra of manganese standards of known oxidation state (Figure S3), it is possible to determine a linear relationship between the edge position and the oxidation state of manganese, which is shown for our samples in Figure 3f. The edge position of each sample's spectrum is extracted by determining the first inflexion point of the spectrum's first derivative (Figure 3e). By relating these to the edge positions of the standards (Figure 3f), the average oxidation state of the samples can be determined to 3.79 +/- 0.06 (sample A), 3.70 +/- 0.06 (sample B) and 3.73 +/- 0.06 (sample C). Assuming that the samples contain only Mn^{3+} and Mn^{4+} species, this corresponds to Mn^{3+} ion fractions of 21 +/- 6 %, 30 +/- 6 %, and 27 +/- 6 % (Table 1). This can be interpreted as the presence of Coleman defects. More Mn^{3+} is thus present in samples synthesised at 80°C (B and C) than in the one synthesised at 120°C (A). Furthermore, a smaller fraction of Mn^{3+} atoms is found in C than in B, i.e. when synthesis time is increased. The XANES data show that the manganese ions are further oxidised as the synthesis is carried out for a longer time, or at higher temperature, resulting in a lower amount of Coleman defects. The results obtained from the XANES data thus agree well with the

trends from the PDF analysis. However, for all three samples, the estimated amount of Mn^{3+} by XANES is higher than the refined weight fraction of γ-MnOOH from PDF (ca. 5 %). This difference will be discussed further below. We note here that the error bars, estimated from the fitting of a Gaussian function to the first maximum of the first derivative of each XANES spectrum, show some overlap between the three samples. However, the similarity in the trends observed between the PDF and XANES results support the validity of the results.

The analysis presented so far enabled us to quantify Coleman defects, but not Ruetschi defects. Since both correspond to the formation of hydroxyl groups within the structure, they can potentially be removed under thermal treatment and tracking their mass loss while performing TGA would allow to quantify both types of defects. TGA shows four major mass losses when the samples are heated to 600 °C as demonstrated in Figure 4. The first one, occurring below 150°C, is assigned to adsorbed water on the surface and is referred to as mass loss 0 in the figure. A second mass loss takes place between 150 °C and 270 °C, labelled step 1 in Figure 4. This can be attributed to the conversion of the MnOOH domains, generated by Coleman defects, to Mn_2O_3 through the release of water molecules, as described by Zhou et al.[25] The reaction can be described as:

$$2\mathrm{MnOOH} \rightarrow \mathrm{Mn_2O_3} + \mathrm{H_2O}\ (1)$$

A steady mass loss (step 2) is observed from 280 °C to 380 °C, which is followed by a steeper one (step 3) up to 580 °C. Since Coleman defects were healed at lower temperatures, we can assign the water loss observed from 280 °C until 420 °C (step 2) to the annealing of Ruetschi defects. The reaction occurring is:

$$\mathrm{Mn_3}V_{Mn}\mathrm{O_4(OH)_4} \rightarrow 3\mathrm{MnO_2} + 2\mathrm{H_2O}\ (2)$$

where V_{Mn} indicates a Mn vacancy. Step 3 can be attributed to the reduction of MnO_2 to Mn_2O_3, as discussed in several reports:[22,47]

$$2\mathrm{MnO_2} \rightarrow \mathrm{Mn_2O_3} + \tfrac{1}{2}\mathrm{O_2}\ (3)$$

We quantified each mass loss for sample A, B, and C, as presented in Table 1. To do so, the difference of mass between the temperatures indicated for each mass loss is determined based on the curves presented in Figure 4. The quantity of related H_2O is then calculated, assuming that only water is produced (expect for mass loss 3 where O_2 is released). This quantity is then related to the quantity of sample (assuming its chemical composition is MnO_2) to estimate the amount of Coleman and Ruetschi defects with respect to equations 1 and 2. Note that the temperature range corresponding to each reaction is not the same for the three samples. Specifically, the mass loss related to the healing of Coleman defects (step 1) happens at in lower temperature range in sample A than in the two others e.g., around 180°C instead of 220°C (see inset in Figure 4). This effect may be related to the presence of microtwinning, which is a known phenomenon in γ-MnO_2 structures.[43] In studies on microtwinning in Fe-doped Sr_2CoMoO_6 nanoparticles, Zhang et al[48] showed mass losses in TGA were shifted towards a lower temperature with higher amounts of microtwinning and may thus be present in sample A. However, at this point this hypothesis is of speculative nature and is not investigated further in this study.

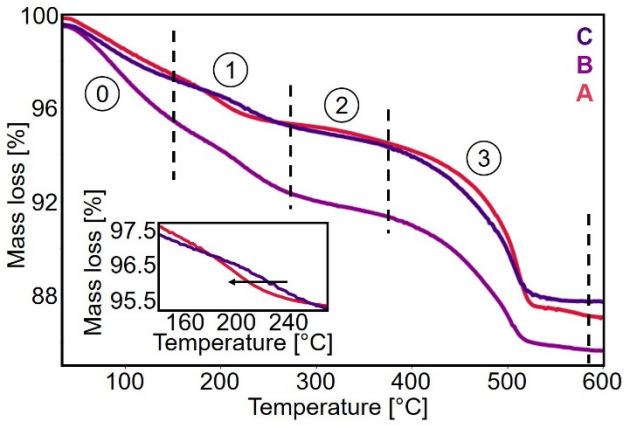

Figure 4: TGA experiments carried out on samples A (2h 120°C), B (3h 80°C) and C (6h 80°C) at a heating rate of 10 K/min under N_2 flow. Mass losses corresponding to 0) the desorption of surface water, dehydroxylation of 1) Coleman defects, 2) Ruetschi defects and 3) the reduction of MnO_2 to Mn_2O_3. The inset shows a magnification of mass loss 2 of samples A and C.

As seen from Table 1, sample A shows a significant mass loss (1 %) at step 2, related to the removal of Ruetschi defects. The same mass loss may be observed, although in a smaller amount (0.3 %), in sample B as well. The results thus suggest that the presence of Ruetschi defects is related to a higher synthesis temperature.

Table 1 furthermore compares the fraction of Coleman defects in sample A, B, and C as determined from PDF, XANES and TGA. Generally, the values of the three methods are in reasonable agreement, and the same trends are seen. However, for sample B and C, the amount of Coleman defects estimated from PDF analysis is lower than the ones from TGA and XANES. While the PDF refinement included only the γ-MnOOH to account for Coleman defects, this may not be the only environment in which Mn^{3+} ions can potentially insert. As discussed above, Coleman defects can be present in both β- and R-MnO_2 parent structures as local γ- and α-MnOOH domains.[12] The higher amount of Coleman defects estimated from the analysis of XANES and TGA data compared to PDF analysis supports that some of the Mn^{3+} ions may be comprised in α-MnOOH domains.

Formation of Coleman and Ruetschi defects

Having established the presence of defects in the material using several techniques, we now consider their formation. The synthesis is performed by reacting $MnSO_4 \cdot H_2O$ with $(NH_4)_2S_2O_8$. The oxidation of Mn^{2+} by $S_2O_8^{2-}$ formally leads to Mn^{4+} as presented in Eq. 4:

$$Mn^{2+} + S_2O_8^{2-} + 2H_2O \longrightarrow MnO_2 + 2SO_4^{2-} + 4H^+ \qquad (4)$$

However, theoretical studies of the formation pathway of MnO_2 suggest that Mn^{3+} ions in the form of MnOOH are present as intermediate species.[11] Increasing the reaction time leads to further oxidation of Mn^{3+} ions into Mn^{4+} and thus MnO_2. Coleman defects in γ-MnO_2 samples may thus form as protons insert into the structure leading to local MnOOH domains, which with time convert into MnO_2. This would explain why we observe less MnOOH domains in the sample synthesised at 80 °C for 6 h compared to the one at 80 °C for 3 h (Table 1). As the temperature increases, the conversion rate is increased, explaining why our sample synthesised at 120°C for 2h (sample A) contains lower amounts of MnOOH domains than the samples synthesised at 80 °C (sample B and C, Table 1).

We only observe Ruetschi defects in a significant amount in sample A, with an estimated amount of Mn vacancies of 3 % (Table 1) in agreement with common ranges of Ruetschi defects found in other γ-MnO_2 samples.[12] While sample A (120 °C) is synthesised above the boiling point of water, samples B and C were synthesised only at 80°C. With increasing temperature point defects are more likely introduced into the structure as the particles form at a faster rate,[49,50] trapping hydroxyl groups around the vacant site.

Defects may be a consequence of fast formation kinetics. It is well known that fast nanoparticle crystallisation at higher synthesis temperatures can lead to more defective structures.[51,52] These defects may anneal as the synthesis is carried out for a longer time and thermal vibrations promote the mobility of the ions.

Table 1: Percentage of mass loss related to reactions (1), (2) and (3) occurring during thermal decomposition of samples A, B and C. Their chemical formula, amount of Mn vacancies and Mn^{3+} is estimated based on the mass losses. The amount of Mn^{3+} estimated from XANES and PDF is summarised as well.

Sample	A	B	C
Mass loss step 1 [150-270°C]: Dehydroxylation of Coleman defects [%]	2.4(1)	3.3(1)	2.3(1)
Mass loss step 2 [270-380°C]: Dehydroxylation of Ruetschi defects [%]	1.0(1)	0.3(1)	0.1(1)
Mass loss step 3 [380-580°C]: Reduction of MnO_2 to Mn_2O_3 [%]	7.5(1)	5.7(1)	6.9(1)
Chemical formula	$Mn^{4+}_{0.75}Mn^{3+}_{0.23}O_2H_{0.33}$	$Mn^{4+}_{0.67}Mn^{3+}_{0.32}O_2H_{0.35}$	$Mn^{4+}_{0.78}Mn^{3+}_{0.22}O_2H_{0.23}$
%Mn vacancy, Ruetschi defects (TGA) [%]	3(1)	1(1)	0(1)
$\%Mn^{3+}$, Coleman defects (TGA) [%]	23(1)	32(1)	22(1)
$\%Mn^{3+}$, Coleman defects (XANES) [%]	21(6)	30(6)	27(6)
$\%Mn^{3+}$, Coleman defects (PDF) [%]	19.2(4)	26.3(5)	21.3(4)

Inelastic neutron scattering and nanostructure analysis

In the sections above, we were able to quantify the two types of H-related defects in γ-MnO_2. However, the presence of H was shown only indirectly. This issue can be alleviated using neutron scattering, since ^1H scatter neutrons strongly compared to oxygen and manganese, allowing to characterise the presence of hydrogen directly. Inelastic neutron scattering spectra were therefore collected for the three samples and are shown in Figure 5a. Bands below 300 cm^{-1} and in the range 500-800 cm^{-1} can be assigned to phonon modes of the Mn-O lattice,[53] and will not be further analysed here. Two sharp bands are seen at 330 and 390 cm^{-1}, which can be assigned to OH stretching, as such bands have also been observed in γ-MnOOH and in H-rich γ-MnO_2 samples by Fillaux et al.[16,32] Since Coleman defects in γ-MnO_2 structures can be related to MnOOH domains, similar bands can be observed in their INS spectra. A broader band is also seen above 1000 cm^{-1}, which can be assigned to Mn-OH vibrations inside the tunnels.[32] The three bands are thus related to the presence of Coleman defects. Since they present similar intensities after normalisation over the probed sample mass, no quantitative information may be extracted from the data. However, in the previously published INS spectra of pure γ-MnOOH, the band at 1000 cm^{-1} (Mn-OH vibration in tunnels) is the strongest, while the bands below 400 cm^{-1} are ten times less intense.[32] We observe the opposite trend in our data (Figure 5a) and relate this to the nanostructure of the material. While the band at 1000 cm^{-1} can be assigned to bulk vibrations of the (OH) groups, the two bands at 330 cm^{-1} and 390 cm^{-1} may be related to surface vibrations. This is confirmed by previous Raman spectroscopy studies,[19,54] where the two bands in the range 300-400 cm^{-1} were specifically assigned to stretches of

surface Mn-OH based on Normal Coordinates analysis. As neutron spectroscopy peak positions can be directly compared to Raman spectroscopy, we suggest assigning these bands to these modes of vibration.

This observation suggests that the Coleman defects are likely present at the surface of the nanoparticles. Previous studies on other systems, e.g. CeO_2 nanoparticles,[55] have shown similar signatures in their INS spectra, i.e. strong bands at low wavenumbers, which have been related to the presence of surface hydrides and hydroxides. This observation can be generalised to other oxides whose surface often show hydroxides.[56-59] Sun et al.[11] have calculated the surface energy of different manganese compounds including oxides and oxyhydroxides, and showed that oxyhydroxide compounds have a smaller surface energy than their oxide analogues. This supports the idea that defect-rich γ-MnO_2 nanoparticles are stabilised by Coleman defects situated at the surface, which lower the surface energy. Furthermore, the manganese ions in the oxyhydroxide phase are in oxidation state +III and therefore show JT distortion of their crystal field, while manganese in oxidation state +IV, i.e. in MnO_2, does not.[42] Strain generating JT distorted [$Mn^{3+}O_6$] octahedra at the surface could thus stabilise defective γ-MnO_2 nanoparticles in a metastable state.[60]

Oxyhydroxide domains at the surface of the nanoparticles with a MnO_2 core implies that the particles can be compared to a core-shell architecture, with a R-MnO_2-type γ-MnO_2 core and a γ-MnOOH-type shell structure. As discussed previously, only the local range of the PDFs, up to 20 Å, could be well modelled using these two phases (Fig 3a-c). Furthermore, the *a* and *b* cell parameters of the refined γ-MnOOH phase are far off compared to bulk γ-MnOOH and much smaller (Table S3).[61] This mismatch could relate to compression stress of the γ-MnOOH-like shell to match the structure of the R-MnO_2-rich core of the particles. Indeed, the refined *b* cell parameter of the γ-MnOOH nearly match the one of R-MnO_2 (4.79 Å vs 4.45 Å), supporting the idea that these two phases connect within a single framework. Since Coleman defects are mostly localised at the surface of the nanoparticles, it is interesting to point out that a thermal treatment removing the corresponding hydroxyl groups through a dehydroxylation reaction would probably yield a surface that is rich in anion-site vacancies. A current trend in the study of γ-MnO_2 is the generation of O-deficient structures for enhancing the availability of metal sites for catalysis.[62-65]

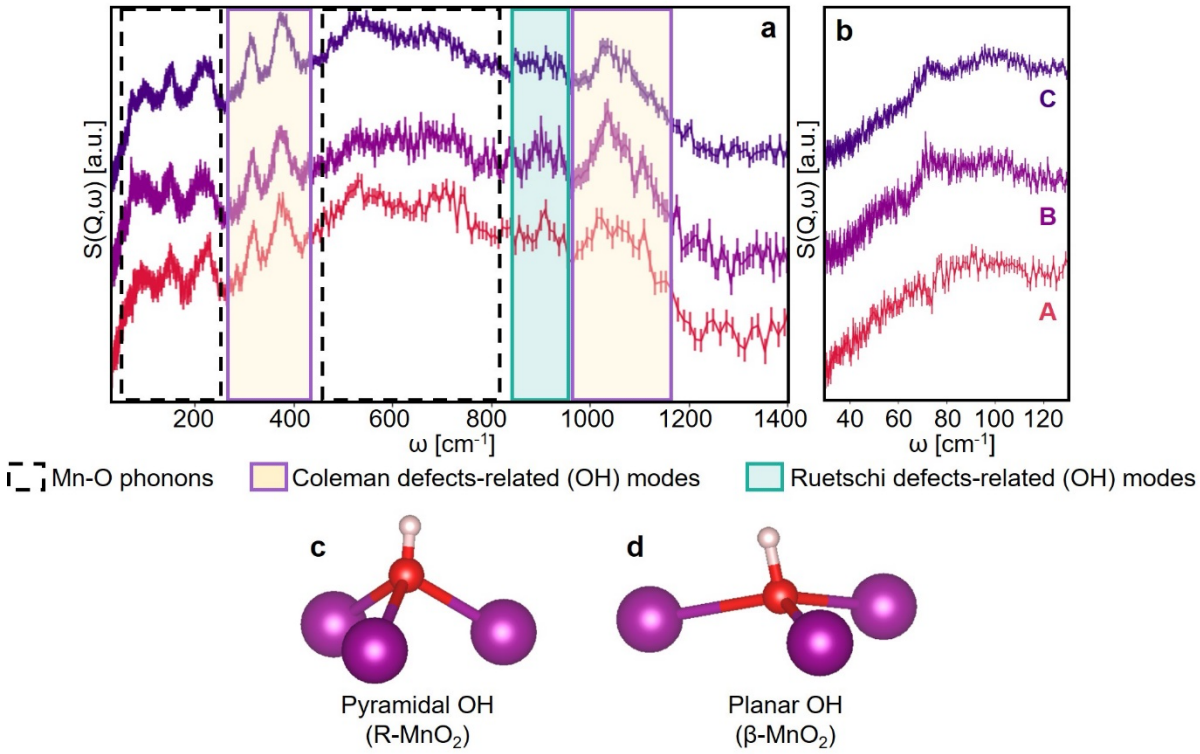

Figure 5: a) INS spectra acquired on samples A (2h 120°C), B (3h 80°C) and C (6h 80°C) at Tosca, ISIS, at 20 K. b) Magnification of the low ω region. Illustration of O atoms in a c) pyramidal and d) planar environment. (Mn atoms shown in purple, O in red and H in white)

Previous INS studies on different manganese oxides, including γ-MnO_2,[32,66,67] have shown that a band around 900 cm^{-1} can be assigned to hydrogen atoms sitting in the vicinity of a vacancy on a manganese site, i.e. a Ruetschi defect. A broad band at this wavenumber is indeed present in the INS data of samples A and B, and an even broader band is observed for sample C, as emphasised in the green area in Figure 5a. At low wavenumbers where bands related to collective motions in the structure are expected, a band at 75 cm^{-1} can be most clearly observed in sample C. This band is broader in sample B and nearly absent in sample A (Figure 5b). This implies that phonon propagation in B and A is hampered by discontinuities in the periodic lattice e.g., by point defects such as Ruetschi defects, in contrast to C. As such, the INS data supports the findings from the TGA analysis that Ruetschi defects are present in sample A and B but absent in C. The data thus supports the idea that Ruetschi defects form at an early stage of the crystallisation of MnO_2, which tend to be annealed with time. The structure then reorganises into a more ordered state when the synthesis is carried out for a longer time. Concerning the location of Ruetschi defects, it is less evident whether they are located in the "core" MnO_2 structure or in the MnOOH-like "shell". However, Ruetschi defects are known to be more stable in the R-MnO_2 than in the β-MnO_2 structure,[13] as it is more favorable to form hydroxyls in the oxygen pyramidal environment found in R-MnO_2 than in the planar one in the β-MnO_2 rutile structure (Figure 5c-d).[35] As the Coleman defect-rich shell in our nanoparticles is closely related to γ-MnOOH, i.e. a distorted rutile structure structurally related to β-MnO_2, it is thus more likely that the Ruetschi defects are located mainly in the R-MnO_2-type core.

The INS data in Figure 5a furthermore show an inverse correlation between the sharpness of the band at 900 cm^{-1} (related to Ruetschi defects) and the broadening of the band above 1000 cm^{-1} (related to Coleman defects) for the three samples. It has previously been suggested that Coleman and Ruetschi defects interact,[32] causing a gradual red-shift in the position of the band above 1000 cm^{-1} when a (OH) group from a Coleman defect is closer to a Ruetschi defect. One can argue that the more Ruetschi defects are present

in the structure, the more likely is their interaction with the Coleman defect-rich shell of the nanoparticles. The overlap of many bands with various red-shifts could explain the broadening of the band above 1000 cm^{-1} observed in A and to a lesser extent in B. Based on the INS data, we can thus hypothesise that Ruetschi defects might be sitting in the outer part of the R-MnO_2 core and close to the Coleman defect-rich shell of the particles. This is a reasonable assumption as vacancies might act as a buffer to mitigate strains generated between the Mn^{3+} shell and Mn^{4+} core, caused by JT distortions. Eventually, vacancies might even compensate a possible mismatch between the core and shell structures, as has been suggested by Turner et al. using HRTEM imaging to investigate natural γ-MnO_2 samples.[68]

Conclusion

We have shown that it is possible to control the amount and type of hydrogen-related defects formed in R-MnO_2-like γ-MnO_2 nanoparticles by varying time and temperature of a simple hydrothermal synthesis. The combination of several characterisation techniques, namely PDF, XANES, TGA and INS, revealed detailed information about the nanostructure of these nanoparticles and their defect density. We have shown that the γ-MnO_2 nanoparticles adopt a core-shell structure with Coleman defects in the shell, i.e. local oxyhydroxide domains. In contrast, the core may contain Ruetschi defects located likely at the boundary between the core and shell. While the amount of Ruetschi defects increases with temperature, the amount of Coleman defects decreases with extended synthesis times. Our results provide a better understanding of defect formation, quantification and location in nanoparticulate γ-MnO_2. This work could open the way for an optimisation of the number of available metal sites and defects through the selection of specific synthesis conditions and a subsequent thermal treatment.

Acknowledgements

This work is part of a project that has received funding from the European Research Council (ERC) under the European Union's Horizon 2020 Research and Innovation Programme (grant agreement No. 804066). We are grateful to the Villum Foundation for financial support through a Villum Young Investigator grant (VKR00015416). Funding from the Danish Ministry of Higher Education and Science through the SMART Lighthouse is gratefully acknowledged. We acknowledge MAX IV Laboratory for time on Beamline DanMAX under Proposal 20200731. Research conducted at MAX IV is supported by the Swedish Research Council under contract 2018-07152, the Swedish Governmental Agency for Innovation Systems under contract 2018-04969, and Formas under contract 2019-02496. DanMAX is funded by the NUFI grant no. 4059-00009B. We acknowledge the *Center for X-ray Spectroscopy* for providing experiment time and support with the HelXAS spectrometer under proposal number [2021-0013]. We thank the STFC Rutherford Appleton Laboratory for remote access to the TOSCA beamline via beam time proposal RB2090124. AK gratefully acknowledges the Deutsche Forschungsgemeinschaft (DFG, German Science Foundation) for funding of the project Ki 2427/1-1 (# 429360100).

References

1. Chao, D.; Zhou, W.; Ye, C.; Zhang, Q.; Chen, Y.; Gu, L.; Davey, K.; Qiao, S.-Z., An Electrolytic Zn–MnO2 Battery for High-Voltage and Scalable Energy Storage. *Angew. Chem. Int. Ed.* **2019,** *58* (23), 7823-7828.

2. Chamoun, M.; Brant, W. R.; Tai, C.-W.; Karlsson, G.; Noréus, D., Rechargeability of aqueous sulfate Zn/MnO2 batteries enhanced by accessible Mn2+ ions. *Energy Storage Mater.* **2018,** *15*, 351-360.

3. Shin, J.; Seo, J. K.; Yaylian, R.; Huang, A.; Meng, Y. S., A review on mechanistic understanding of MnO2 in aqueous electrolyte for electrical energy storage systems. *Int. Mater. Rev.* **2020,** *65* (6), 356-387.

4. Jouanneau, S.; Sarciaux, S.; Le Gal La Salle, A.; Guyomard, D., Influence of structural defects on the insertion behavior of γ-MnO2: comparison of H+ and Li+. *Solid State Ion.* **2001,** *140* (3), 223-232.
5. Zeng, X.; Cheng, G.; Liu, Q.; Yu, W.; Yang, R.; Wu, H.; Li, Y.; Sun, M.; Zhang, C.; Yu, L., Novel Ordered Mesoporous γ-MnO2 Catalyst for High-Performance Catalytic Oxidation of Toluene and o-Xylene. *Ind. Eng. Chem. Res.* **2019,** *58* (31), 13926-13934.
6. Cellier, C.; Ruaux, V.; Lahousse, C.; Grange, P.; Gaigneaux, E. M., Extent of the participation of lattice oxygen from γ-MnO2 in VOCs total oxidation: Influence of the VOCs nature. *Catal. Today* **2006,** *117* (1), 350-355.
7. Lin, H.; Chen, D.; Liu, H.; Zou, X.; Chen, T., Effect of MnO2 crystalline structure on the catalytic oxidation of formaldehyde. *Aerosol Air Qual. Res.* **2017,** *17* (4), 1011-1020.
8. Liu, L.; Li, J.; Zhang, H.; Li, L.; Zhou, P.; Meng, X.; Guo, M.; Jia, J.; Sun, T., In situ fabrication of highly active γ-MnO2/SmMnO3 catalyst for deep catalytic oxidation of gaseous benzene, ethylbenzene, toluene, and o-xylene. *J. Hazard. Mater.* **2019,** *362*, 178-186.
9. Robinson, D. M.; Go, Y. B.; Mui, M.; Gardner, G.; Zhang, Z.; Mastrogiovanni, D.; Garfunkel, E.; Li, J.; Greenblatt, M.; Dismukes, G. C., Photochemical water oxidation by crystalline polymorphs of manganese oxides: structural requirements for catalysis. *J. Am. Chem. Soc.* **2013,** *135* (9), 3494-501.
10. Lian, S.; Browne, M. P.; Domínguez, C.; Stamatin, S. N.; Nolan, H.; Duesberg, G. S.; Lyons, M. E.; Fonda, E.; Colavita, P. E., Template-free synthesis of mesoporous manganese oxides with catalytic activity in the oxygen evolution reaction. *Sustain. Energy Fuels* **2017,** *1* (4), 780-788.
11. Sun, W.; Kitchaev, D. A.; Kramer, D.; Ceder, G., Non-equilibrium crystallization pathways of manganese oxides in aqueous solution. *Nat. Commun.* **2019,** *10* (1), 573.
12. Kitchaev, D. A.; Dacek, S. T.; Sun, W.; Ceder, G., Thermodynamics of Phase Selection in MnO2 Framework Structures through Alkali Intercalation and Hydration. *J. Am. Chem. Soc.* **2017,** *139* (7), 2672-2681.
13. Balachandran, D.; Morgan, D.; Ceder, G.; van de Walle, A., First-principles study of the structure of stoichiometric and Mn-deficient MnO2. *J. Solid State Chem.* **2003,** *173* (2), 462-475.
14. Ruetschi, P., Cation-Vacancy Model for MnO[sub 2]. *J. Electrochem. Soc.* **1984,** *131* (12), 2737.
15. Vasiliev, I.; Magar, B. A.; Duay, J.; Lambert, T. N.; Chalamala, B., Ab Initio Studies of Hydrogen Ion Insertion into β-, R-, and γ-MnO2 Polymorphs and the Implications for Shallow-Cycled Rechargeable Zn/MnO2 Batteries. *J. Electrochem. Soc.* **2018,** *165* (14), A3517-A3524.
16. Fillaux, F.; Ouboumour, H.; Tomkinson, J.; Yu, L. T., An inelastic neutron scattering study of the proton dynamics in γ-MnO2. *Chem. Phys.* **1991,** *149* (3), 459-469.
17. Hahn, B. P.; Long, J. W.; Rolison, D. R., Something from Nothing: Enhancing Electrochemical Charge Storage with Cation Vacancies. *Acc. Chem. Res.* **2013,** *46* (5), 1181-1191.
18. Balachandran, D.; Morgan, D.; Ceder, G., First Principles Study of H-insertion in MnO2. *J. Solid State Chem.* **2002,** *166* (1), 91-103.
19. Smith, P. F.; Deibert, B. J.; Kaushik, S.; Gardner, G.; Hwang, S.; Wang, H.; Al-Sharab, J. F.; Garfunkel, E.; Fabris, L.; Li, J.; Dismukes, G. C., Coordination Geometry and Oxidation State Requirements of Corner-Sharing MnO6 Octahedra for Water Oxidation Catalysis: An Investigation of Manganite (γ-MnOOH). *ACS Catal.* **2016,** *6* (3), 2089-2099.
20. Park, S.; Lee, Y. H.; Choi, S.; Seo, H.; Lee, M. Y.; Balamurugan, M.; Nam, K. T., Manganese oxide-based heterogeneous electrocatalysts for water oxidation. *Energy Environ. Sci.* **2020,** *13* (8), 2310-2340.
21. Morgan Chan, Z.; Kitchaev, D. A.; Nelson Weker, J.; Schnedermann, C.; Lim, K.; Ceder, G.; Tumas, W.; Toney, M. F.; Nocera, D. G., Electrochemical trapping of metastable Mn3+ ions for activation of MnO2 oxygen evolution catalysts. *Proc. Natl. Acad. Sci.* **2018,** *115* (23), E5261-E5268.
22. Wesley, M. D.; Scott, W. D., Kinetic analysis of γ-MnO2 thermal treatment. *J. Therm. Anal. Calorim.* **2011,** *105* (1), 113-122.

23. Christensen, P. A.; Attidekou, P. S.; Egdell, R. G.; Maneelok, S.; Manning, D. A. C., An in situ FTIR spectroscopic and thermogravimetric analysis study of the dehydration and dihydroxylation of SnO2: the contribution of the (100), (110) and (111) facets. *PCCP* **2016,** *18* (33), 22990-22998.
24. Lee, J.; Ju, J. B.; Cho, W. I.; Cho, B. W.; Oh, S. H., Todorokite-type MnO2 as a zinc-ion intercalating material. *Electrochim. Acta* **2013,** *112*, 138-143.
25. Zhou, F.; Zhao, X.; Yuan, C.; Xu, H., Synthesis of γ-MnOOH nanorods and their isomorphous transformation into β-MnO2 and α-Mn2O3 nanorods. *J. Mater. Sci.* **2007,** *42* (24), 9978-9982.
26. Parker, S. F.; Williams, K. P. J.; Bortz, M.; Yvon, K., Inelastic Neutron Scattering, Infrared, and Raman Spectroscopic Studies of Mg2FeH6 and Mg2FeD6. *Inorg. Chem.* **1997,** *36* (23), 5218-5221.
27. Bantignies, J. L.; Deabate, S.; Righi, A.; Rols, S.; Hermet, P.; Sauvajol, J. L.; Henn, F., New Insight into the Vibrational Behavior of Nickel Hydroxide and Oxyhydroxide Using Inelastic Neutron Scattering, Far/Mid-Infrared and Raman Spectroscopies. *J. Phys. Chem. C* **2008,** *112* (6), 2193-2201.
28. Billinge, S. J. L., The atomic pair distribution function: past and present. *Z. Kristallogr. Cryst. Mater.* **2004,** *219* (3), 117-121.
29. Galliez, K.; Deniard, P.; Petit, P.-E.; Lambertin, D.; Bart, F.; Jobic, S., Modelling and quantification of intergrowth in γ-MnO2by laboratory pair distribution function analysis. *J. Appl. Crystallogr.* **2014,** *47* (2), 552-560.
30. Magnard, N. P. L.; Anker, A. S.; Aalling-Frederiksen, O.; Kirsch, A.; Jensen, K. M. Ø., Characterisation of intergrowth in metal oxide materials using structure-mining: the case of γ-MnO2. *Dalton Trans.* **2022,** *51* (45), 17150-17161.
31. Ripert, M.; Pannetier, J.; Chabre, Y.; Poinsignon, C., Manganese Dioxides: Structural Model and In-Situ Neutron Powder Diffraction Investigation of Thermal Annealing and Electrochemical Reduction. *MRS Proc.* **1990,** *210*, 359.
32. Fillaux, F.; Cachet, C. H.; Ouboumour, H.; Tomkinson, J.; Lévy-Clément, C.; Yu, L. T., Inelastic Neutron Scattering Study of the Proton Dynamics in Manganese Oxides: I . and Manganite. *J. Electrochem. Soc.* **1993,** *140* (3), 585-591.
33. Manceau, A.; Marcus, M. A.; Grangeon, S., Determination of Mn valence states in mixed-valent manganates by XANES spectroscopy. *Am. Mineral.* **2012,** *97* (5-6), 816-827.
34. Galliez, K.; Deniard, P.; Payen, C.; Lambertin, D.; Bart, F.; Koo, H.-J.; Whangbo, M.-H.; Jobic, S., Pair Distribution Function and Density Functional Theory Analyses of Hydrogen Trapping by γ-MnO2. *Inorg. Chem.* **2015,** *54* (4), 1194-1196.
35. Morgan, D.; Balachandran, D.; Ceder, G.; van de Walle, A., A Drastic Influence of Point Defects on Phase Stability in MnO2. *MRS Proc.* **2002,** *755*, DD2.8.
36. Wang, X.; Li, Y., Selected-Control Hydrothermal Synthesis of α- and β-MnO2 Single Crystal Nanowires. *J. Am. Chem. Soc.* **2002,** *124* (12), 2880-2881.
37. Prescher, C.; Prakapenka, V. B., DIOPTAS: a program for reduction of two-dimensional X-ray diffraction data and data exploration. *High Press. Res.* **2015,** *35* (3), 223-230.
38. Yang, X.; Juhas, P.; Farrow, C. L.; Billinge, S. J. L., xPDFsuite: an end-to-end software solution for high throughput pair distribution function transformation, visualization and analysis. *eprint arXiv:1402.3163* **2014**, arXiv:1402.3163.
39. Coelho, A. A., TOPAS and TOPAS-Academic: an optimization program integrating computer algebra and crystallographic objects written in C++. *J. Appl. Crystallogr.* **2018,** *51* (1), 210-218.
40. Honkanen, A.-P.; Ollikkala, S.; Ahopelto, T.; Kallio, A.-J.; Blomberg, M.; Huotari, S., Johann-type laboratory-scale x-ray absorption spectrometer with versatile detection modes. *Rev. Sci. Instrum.* **2019,** *90* (3), 033107.
41. Parker, S. F.; Fernandez-Alonso, F.; Ramirez-Cuesta, A. J.; Tomkinson, J.; Rudić, S.; Pinna, R. S.; Gorini, G.; Castañon, J. F., Recent and future developments on TOSCA at ISIS. *J. Phys.: Conf. Ser.* **2014,** *554* (1), 012003.

42. Kim, H.; Yoon, G.; Park, I.; Park, K.-Y.; Lee, B.; Kim, J.; Park, Y.-U.; Jung, S.-K.; Lim, H.-D.; Ahn, D.; Lee, S.; Kang, K., Anomalous Jahn–Teller behavior in a manganese-based mixed-phosphate cathode for sodium ion batteries. *Energy Environ. Sci.* **2015,** *8* (11), 3325-3335.
43. Chabre, Y.; Pannetier, J., Structural and electrochemical properties of the proton / γ-MnO2 system. *Prog. Solid State Chem.* **1995,** *23* (1), 1-130.
44. Figueroa, S. J.; Requejo, F. G.; Lede, E. J.; Lamaita, L.; Peluso, M. A.; Sambeth, J. E., XANES study of electronic and structural nature of Mn-sites in manganese oxides with catalytic properties. *Catal. Today* **2005,** *107*, 849-855.
45. Wong, J.; Lytle, F.; Messmer, R.; Maylotte, D., K-edge absorption spectra of selected vanadium compounds. *Phys. Rev. B* **1984,** *30* (10), 5596.
46. Berry, A. J.; O'Neill, H. S. C.; Jayasuriya, K. D.; Campbell, S. J.; Foran, G. J., XANES calibrations for the oxidation state of iron in a silicate glass. *Am. Mineral.* **2003,** *88* (7), 967-977.
47. Dose, W. M.; Sharma, N.; Webster, N. A. S.; Peterson, V. K.; Donne, S. W., Kinetics of the Thermally-Induced Structural Rearrangement of γ-MnO2. *J. Phys. Chem. C* **2014,** *118* (42), 24257-24265.
48. Zhang, W.; Wang, H.; Guan, K.; Meng, J.; Wei, Z.; Liu, X.; Meng, J., Enhanced Anode Performance and Coking Resistance by In Situ Exsolved Multiple-Twinned Co–Fe Nanoparticles for Solid Oxide Fuel Cells. *ACS Appl. Mater. Interfaces* **2020,** *12* (1), 461-473.
49. Kumari, L.; Li, W. Z.; Xu, J. M.; Leblanc, R. M.; Wang, D. Z.; Li, Y.; Guo, H.; Zhang, J., Controlled Hydrothermal Synthesis of Zirconium Oxide Nanostructures and Their Optical Properties. *Cryst. Growth Des.* **2009,** *9* (9), 3874-3880.
50. Lin, J.; Yang, Z.; Zhao, X.; Ji, H.; Peng, C.; Sui, B.; Chen, W.; Zhang, J.; Qian, G.; Zhou, X.; Duan, X., Kinetics and mechanistic insights into the hydrothermal synthesis of alumina microrods. *Chem. Eng. Sci.* **2021,** *244*, 116817.
51. Dickinson, S. R.; Henderson, G.; McGrath, K., Controlling the kinetic versus thermodynamic crystallisation of calcium carbonate. *J. Cryst. Growth* **2002,** *244* (3-4), 369-378.
52. Tao, H.; Gao, F.; Gao, H.; Hu, W., Free energy change of crystallisation in single copolymers. *Mol. Phys.* **2018,** *116* (21-22), 3020-3026.
53. Post, J. E.; McKeown, D. A.; Heaney, P. J., Raman spectroscopy study of manganese oxides: Tunnel structures. *Am. Mineral.* **2020,** *105* (8), 1175-1190.
54. Cua, A.; Vrettos, J. S.; de Paula, J. C.; Brudvig, G. W.; Bocian, D. F., Raman spectra and normal coordinate analyses of low-frequency vibrations of oxo-bridged manganese complexes. *J. Biol. Inorg. Chem* **2003,** *8* (4), 439-451.
55. Wu, Z.; Cheng, Y.; Tao, F.; Daemen, L.; Foo, G. S.; Nguyen, L.; Zhang, X.; Beste, A.; Ramirez-Cuesta, A. J., Direct neutron spectroscopy observation of cerium hydride species on a cerium oxide catalyst. *J. Am. Chem. Soc.* **2017,** *139* (28), 9721-9727.
56. McInroy, A. R.; Lundie, D. T.; Winfield, J. M.; Dudman, C. C.; Jones, P.; Parker, S. F.; Lennon, D., The interaction of alumina with HCl: An infrared spectroscopy, temperature-programmed desorption and inelastic neutron scattering study. *Catal. Today* **2006,** *114* (4), 403-411.
57. Loong, C.-K.; Rey, C.; Kuhn, L.; Combes, C.; Wu, Y.; Chen, S.-H.; Glimcher, M., Evidence of hydroxyl-ion deficiency in bone apatites: an inelastic neutron-scattering study. *Bone* **2000,** *26* (6), 599-602.
58. Spencer, E. C.; Levchenko, A. A.; Ross, N. L.; Kolesnikov, A. I.; Boerio-Goates, J.; Woodfield, B. F.; Navrotsky, A.; Li, G., Inelastic neutron scattering study of confined surface water on rutile nanoparticles. *J. Phys. Chem. A* **2009,** *113* (12), 2796-2800.
59. Loong, C. K.; Richardson, J. W.; Ozawa, M., Crystal Phases, Defects, and Dynamics of Adsorbed Hydroxyl Groups and Water in Pure and Lanthanide-Modified Zirconia: A Neutron-Scattering Study. *J. Catal.* **1995,** *157* (2), 636-644.

60. Liu, Y.; Wang, C.; Zhao, S.; Zhang, L.; Zhang, K.; Li, F.; Chen, J., Mitigation of Jahn–Teller distortion and Na+/vacancy ordering in a distorted manganese oxide cathode material by Li substitution. *Chem. Sci.* **2021,** *12* (3), 1062-1067.
61. Kohler, T.; Armbruster, T.; Libowitzky, E., Hydrogen Bonding and Jahn–Teller Distortion in Groutite,α-MnOOH, and Manganite,γ-MnOOH, and Their Relations to the Manganese Dioxides Ramsdellite and Pyrolusite. *J. Solid State Chem.* **1997,** *133* (2), 486-500.
62. Zheng, H.; Modibedi, M.; Mathe, M.; Ozoemena, K., The thermal effect on the catalytic activity of MnO2 (α, β, and γ) for oxygen reduction reaction. *Mater. Today: Proceedings* **2017,** *4* (11, Part 2), 11624-11629.
63. Huo, G.; Wang, X.-W.; Zhang, Z.-B.; Song, Z.; Kang, X.-M.; Chen, M.-X.; Wang, Q.; Fu, X.-Z.; Luo, J.-L., γ-MnO2 nanorod-assembled hierarchical micro-spheres with oxygen vacancies to enhance electrocatalytic performance toward the oxygen reduction reaction for aluminum-air batteries. *J. Energy Chem.* **2020,** *51*, 81-89.
64. Cheng, F.; Zhang, T.; Zhang, Y.; Du, J.; Han, X.; Chen, J., Enhancing Electrocatalytic Oxygen Reduction on MnO2 with Vacancies. *Angew. Chem. Int. Ed.* **2013,** *52* (9), 2474-2477.
65. Zhuang, Q.; Ma, N.; Yin, Z.; Yang, X.; Yin, Z.; Gao, J.; Xu, Y.; Gao, Z.; Wang, H.; Kang, J.; Xiao, D.; Li, J.; Li, X.; Ma, D., Rich Surface Oxygen Vacancies of MnO2 for Enhancing Electrocatalytic Oxygen Reduction and Oxygen Evolution Reactions. *Adv. Energy Sustainability Res.* **2021,** *2* (8), 2100030.
66. Fillaux, F.; Ouboumour, H.; Cachet, C. H.; Tomkinson, J.; Lévy-Clément, C.; Yu, L., Inelastic Neutron Scattering Study of the Proton Dynamics in Manganese Oxides: II. Proton Insertion in Electrodeposited. *J. Electrochem. Soc.* **1993,** *140* (3), 592.
67. Aitchison, P.; Ammundsen, B.; Bell, T.; Jones, D.; Roziere, J.; Burns, G.; Berg, H.; Tellgren, R.; Thomas, J., Proton insertion in spinel lithium manganates and the effect of manganese substitution. *Physica B Condens. Matter* **2000,** *276*, 847-848.
68. Turner, S.; Buseck, P. R., Defects in nsutite (γ-MnO 2) and dry-cell battery efficiency. *Nature* **1983,** *304* (5922), 143-146.